2010

Hyperspectral Methods of Determining Grit Application Density on Sandpaper

Lee A. Clark
Wright State University

HYPERSPECTRAL METHODS OF DETERMINING

GRIT APPLICATION DENSITY ON SANDPAPER

A thesis submitted in partial fulfillment
of the requirements for the degree of
Master of Science in Engineering

By

Lee Allen Clark
M.A., The Kent State University, 1993
B.S., The Ohio State University, 1989

2010
Wright State University

WRIGHT STATE UNIVERSITY

SCHOOL OF GRADUATE STUDIES

FEBRUARY 23, 2010

I HEREBY RECOMMEND THAT THE THESIS PREPARED UNDER MY SUPERVISION BY LEE ALLEN CLARK ENTITLED HYPERSPECTRAL METHODS FOR DETERMINING GRIT APPLICATION DENSITY ON SANDPAPER BE ACCEPTED IN PARTIAL FULFILLMENT OF THE REQUIREMENTS FOR THE DEGREE OF Master of Science in Engineering

Kefu Xue, Ph.D.
Thesis Director
Department Chair

Committee on
Final Examination

Fred Garber, Ph.D.

Lang Hong, Ph.D.

Arnab Shaw, Ph.D.

Jack A. Bantle, Ph.D.
Vice President for Research and
Graduate Studies and Interim Dean
of Graduate Studies

ABSTRACT

Clark, Lee Allen. M.S.Egr., Department of Electrical Engineering, Wright State University, 2010. Hyperspectral Methods for Determining Grit Application Density on Sandpaper.

A low cost real time method of determining the density of grit applied to sandpaper does not currently exist. This thesis will explore three methods for determining grit density from digital image data. A means to characterize the application in terms of frequency by using direct cosine transform basis images will be explored. An RX detector algorithm to characterize the image background will be tested. A linear unmixing methodology will be developed that characterizes the proportion of glue and grit present in each hyperspectral pixel vector.

TABLE OF CONTENTS

LIST OF FIGURES

Number *Page*

ACKNOWLEDGMENTS

The author wishes to express sincere appreciation to Professor Kefu Xue for his assistance in the preparation of this manuscript. In addition, special thanks to Chris Ali and Ali Industries for their support and Gail Kittleson whose knowledge of the abrasive industry was critical to the planning of the project.

CHAPTER 1-GRIT DENSITY BACKGROUND AND THE STATE OF THE ART

GRIT APPLICATION

Typically grit particles are applied to sandpaper by means of an electrostatic process that causes the particles to leap from a negatively charged vibrating conveyor to a positive charged electrode. A continuous sheet of paper with a layer of wet glue is passed between the conveyor and the electrode intercepting the grit particles. The grit particles become embedded in the glue on the sheet of paper. The electrostatic process aligns the grit particles such that the particles are optimally arranged for cutting.

Several factors affect the density of the grit application. The electrode voltage, conveyor speed, and conveyor vibration magnitude must be adjusted to achieve the proper grit application density. The machine operator must fine tune these adjustments to deliver the required sandpaper quality.

Grit applied too sparsely creates an obvious sandpaper quality issue. But grit applied too thickly can cause quality issues as well. The over application of grit particles also adds unnecessary cost to the final sandpaper product.

GRIT DENSITY MEASUREMENT

Grit density measurement techniques have been developed to help sandpaper making machinery operators verify the quality of the sandpaper being produced.

VISUAL INSPECTION

Microscopes are typically used by operators to assess the density and quality of the grit application. The microscopes do not provide quantitative feedback but they do provide a means for operators to perform a basic assessment of the quality of a sandpaper sample.

If grit particles are applied too heavily the particles do not align their cutting surface properly. Through visual inspection the operator can detect the orientation of the grit particles.

RADIATION BASED DENSITY MEASUREMENT

Sandpaper density sensors that use radiation have been employed by many sandpaper manufacturers. The radiation based sensors measure the amount of radiation reflected or passed through the sandpaper. The sensor readings are compared to a known standard for the product to determine the grit density.

The radiation based sensors are problematic for a few reasons. The radiation sensors typically cost in excess of $100,000. The sensors may require government approval for use due to the radiation emission. The sensor calibration requires frequent adjustment. The maintenance of a database of acceptable sensor readings for each product can be difficult for a sandpaper manufacturer with potentially hundreds of different products that are subject to recipe changes at any time.

STANDARD WEIGHT BASED DENSITY MEASUREMENT

Many manufacturers use weight based measurements to monitor the quality of the sandpaper making process. Precise shapes are cut from samples of plain paper, paper with glue, paper with glue and grit. The weight of the samples is used to determine how much grit in terms of weight has been applied to the sandpaper.

Weight based processes are relatively cheap and easy to implement but the frequency of measurement is somewhat limited. Many meters of sandpaper could be produced before a grit application issue is identified by the operator.

IMAGE BASED GRIT DENSITY MEASUREMENT

Image based grit density measurement provides many opportunities for improvement over existing grit density measurement techniques. The cost of strobe lighting and a high shutter speed camera is an order of magnitude less expensive than a radiation based measurement system. The instantaneous feedback and increased measurement frequency that an image based system could provide would be an advantage over a weight based measurement.

CHAPTER 2 -DATA COLLECTION AND CALIBRATION

SAMPLE COLLECTION

Samples of varying grit density were collected and pasted on to boards to keep the samples flat. The samples were then photographed with a hyperspectral camera supplied by The Wright Patterson Air Force Base. The hyperspectral camera captured 120 wavelengths from 394.2 nm to 893.9 nm. The following sandpaper samples were imaged:

1	Urea Glue on Paper, Base for Samples 2 and 3
2	50 Grit on Paper, AO with Urea, 1.67 gm
3	50 Grit on Paper, AO with Urea, 1.86 gm
4	Urea Glue on Paper, Base for Samples 5 and 6
5	40 Grit on Paper, AO with Urea, 2.52 gm
6	40 Grit on Paper, AO with Urea, 3.43 gm
7	Phenolic Glue on Cloth, Base for Samples 9 and 10
8	80 Grit on Cloth, AO with Phenolic, 1.31 gm
9	80 Grit on Cloth, AO with Phenolic, 1.84 gm
10	120 Grit on Paper, Z and AO with Phenolic, .573 gm
11	120 Grit on Paper, Z and AO with Phenolic, .883 gm
12	120 Grit on Paper, Z and AO with Phenolic, 1.1 gm
13	
14	
15	White Calibration Board
16	Gray Calibration Board

The images were captured in direct sun light. A laptop computer was used to adjust the exposure. The bright sunlight made the laptop screen extremely difficult for viewing and consequently some images were under exposed.

CAMERA RESOLUTION AND GRIT PARTICLE SIZE

The samples were 115 mm diameter circles. The number of camera pixels across the diameter of the sample was approximately 550 pixels. The resulting pixel size was approximately .21 mm x .21 mm.

During the manufacture of Aluminum Oxide abrasive, the Aluminum Oxide is crushed to form small particles. The particles have a wide range of sizes. Filters are used to limit the maximum particle size for each of the different grit ratings. For example, the maximum particle size for 80 grit sandpaper is typically near .25 mm. However, Aluminum Oxide abrasive used for 80 grit sandpaper also contains a wide range of particles small than .25 mm in length.

For our four grit samples, 40 grit, 50 grit, 80 grit, and 120 grit, the maximum particle size is nearly equal to if not larger than the pixel size of the images. However, fine Aluminum Oxide particles can fill in areas between the larger grit particles. The fine particles can be much smaller than the pixel size. As the following magnified image of sandpaper indicates, areas that are primarily glue can contain small particles of Aluminum Oxide dust.

EMPIRICAL LINE METHOD CAMERA CALIBRATION

The empirical line calibration method as described by Geoffrey M. Smith and Edward J. Milton was used to calibrate the hyperspectral image data. The empirical line method uses two calibration points to form a linear predictor of camera recorded radiance versus surface reflectance. In our case, gray and white calibration targets with specified surface reflectance were compared to the camera radiance values to generate slope and intercept values for each of the hyperspectral camera wavelengths.

The calibrated reflectance of any camera radiance reading can be calculated as follows:

$R = sL+i$

Where R = Reflectance, s = slope, L = Camera Radiance, i = intercept

AVERAGE CALIBRATION PANEL SURFACE REFLECTANCE

The following calibration reflectance readings were provided for the gray calibration panel and the white calibration panel.

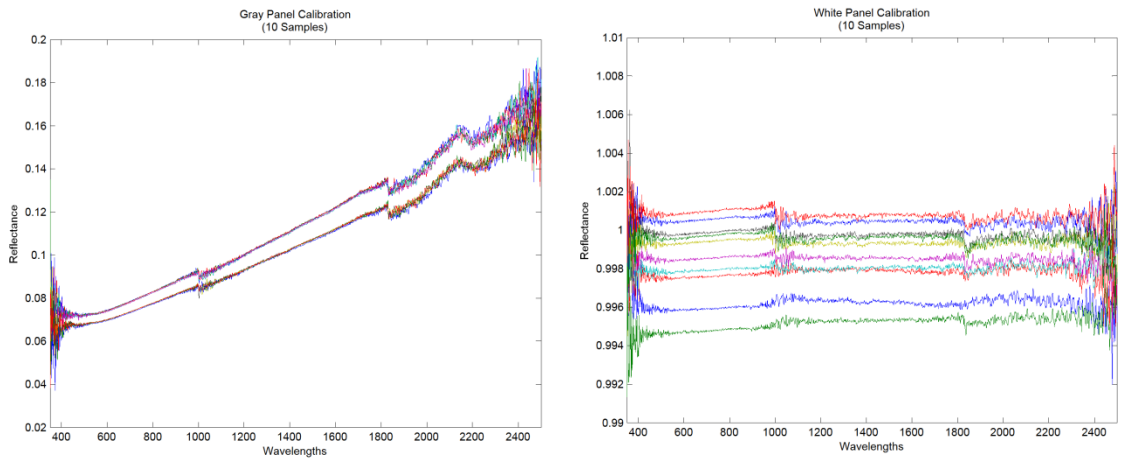

FIGURE 1- GRAY PANEL AND WHITE PANE CALIBRATION DATA

The 10 calibration samples for both the gray calibration panel and the white calibration panel were averaged to provide a single set of reflectance calibration values.

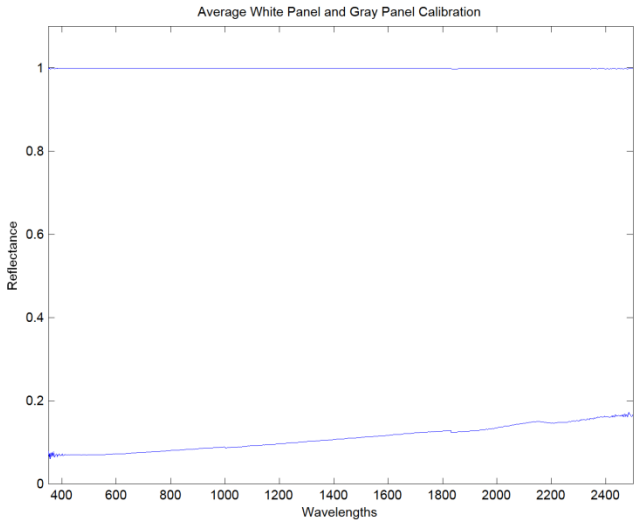

FIGURE 2- AVERAGE WHITE AND GRAY CALIBRATION

HYPERSPECTRAL CAMERA AVERAGE CALIBRATION PANEL RADIANCE

It is possible to calibrate each pixel individually. The calibration panel image does not cover the entire camera field of view. So, the calibration will be averaged over a 36 pixels in the middle of the camera image. Each camera pixel will be treated equally.

The following average gray panel and white panel radiance readings were averaged from a region in the center of the camera image.

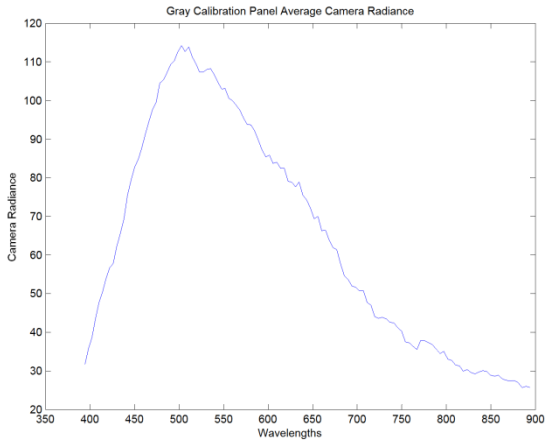

FIGURE 3- GRAY CALIBRATION PANEL AVERAGE CAMERA REFLECTANCE

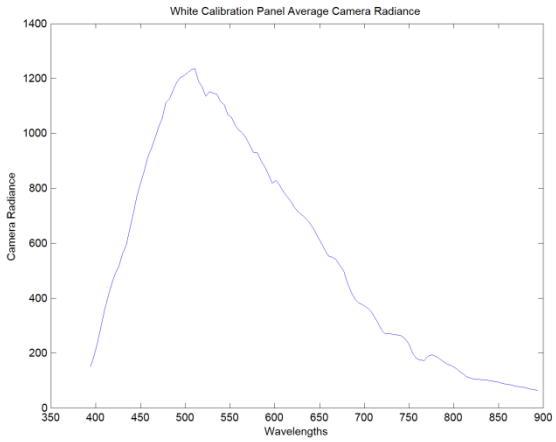

FIGURE 4- WHITE CALIBRATION PANEL AVERAGE CAMERA REFLECTANCE

EMPIRICAL LINE METHOD SLOPE AND INTERCEPT CALCULATIONS

The hyperspectral camera data wavelengths do not match the calibration wavelengths provided for the gray and white calibration panels. A linear interpolation must be performed to find appropriate calibration panel reflectance readings for the hyperspectral camera wavelengths.

The slope is calculated as follows:

Slope = (WhitePanelReflectance-GrayPanelReflectance)/(CameraAvgWhite-CameraAvgGray)

After the slope is calculated, the Y intercept can be computed as follows:

*Intercept = GrayPanelReflectance- Slope*CameraAvgGray*

The slope and intercept calculations are performed for each of the hyperspectral camera wavelengths. Images can then be calibrated by multiplying each of the camera readings by the slope and adding the Y intercept.

IMAGES CALIBRATED WITH EMPIRICAL LINE METHOD

After the calibration slope and intercept values are calculated for each of the camera's wavelengths, the camera image can be calibrated. Each of the 120 radiance values for every pixel should multiplied by the slope and the result added to the intercept.

Calibrated Reflectance = (Camera Radiance x Slope) + Intercept

The following is an example of an original camera image and the calibrated image. The images have been converted to an RGB format.

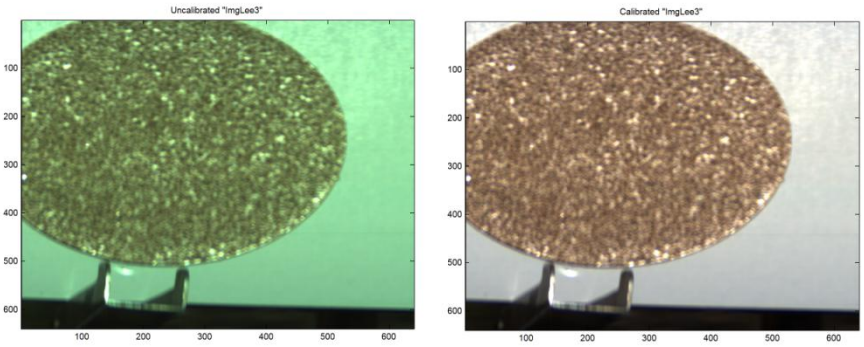

FIGURE 5 - UNCALIBRATED AND CALIBRATED IMAGE OF SANDPAPER SAMPLE

CHAPTER 3 - DIRECT COSINE TRANSFORM

CHARACTERIZATION OF GRIT APPLICATION

If the density of grit on sandpaper can be measured by the frequency of transitions from glue to grit in the image, then a technique for characterizing the frequency in an image may be useful.

The direct cosine transform (DCT) characterizes a square section of a two dimensional image as a combination of basis images. The basis images range from DC to high frequency. The amount of contribution of the high frequency images should provide an indication of the rate of transitions from glue to girt in the sandpaper sample.

The following chart shows a set of 8x8 DCT basis images. Basis images on diagonal lines from upper right to lower left have varying orientation. However, the diagonal set of basis images has constant frequency. Summing the magnitude of the contribution of each basis image along the diagonals should capture the contribution of each frequency.

FIGURE 6 – DCT 8X8 BASIS IMAGES

The DCT data was calculated for each of the 120 bands of hyperspectral data. Then in order to characterize the frequency content of the DCT data, the magnitude of the contribution of basis images on the same diagonal were summed. For example, the magnitude of the basis images (1,3), (2,2), and (3,1) were summed to form a measure of the contribution of that particular frequency. A total of 15 diagonals or frequency bands were calculated. The following mesh plot is an example of the data collected for sample #9.

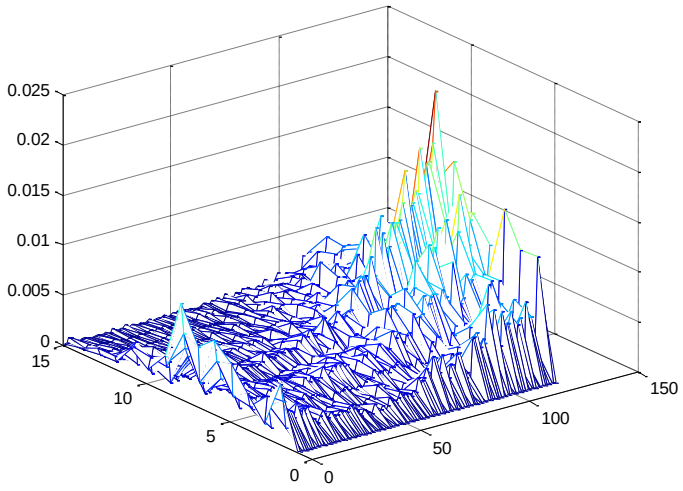

FIGURE 7 - MESH PLOT OF SAMPLE #9 FREQUENCY DIAGONALS

In order to simplify the analysis of the data, the first 25 wavelengths were summed to form a red spectrum contribution, the middle 60 wavelengths were summed to form a green spectrum contribution, and the last 35 wavelengths were summed to form a blue spectrum contribution. The following image shows the combined DCT Diagonal plot of the red, green, and blue wavelength groups.

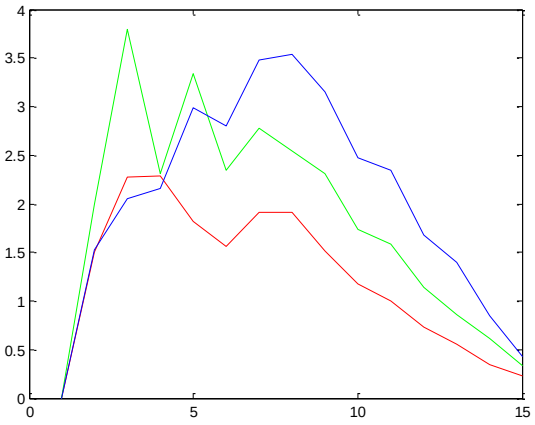

FIGURE 8 - DCT DIAGONAL PLOT FOR RED, GREEN, AND BLUE WAVELENGTH GROUPS

DCT BASIS IMAGE SIZE

DCT basis images of various sizes were explored to determine the optimum size for analysis. The following demonstrates the change in results as the size of the DCT basis image for sample #9 is increased from 4x4 to 256x256.

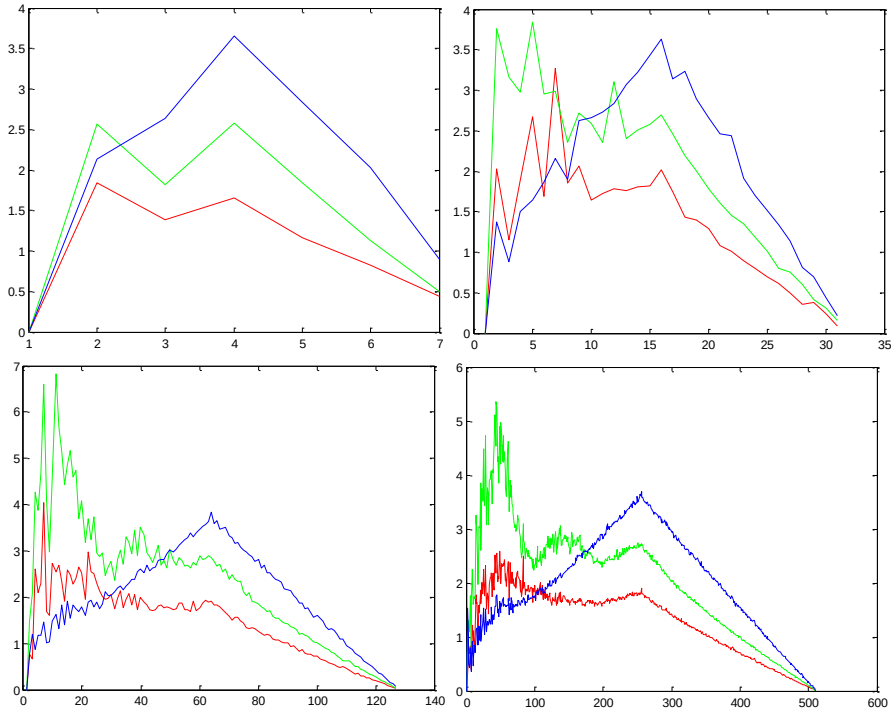

FIGURE 9 - DCT DIAGONALS FOR 4X4, 16X16, 64X64, AND 256X256 BASIS IMAGE SIZES

The shape and magnitude of the DCT diagonals plot appeared consistent across different areas of the sample when the basis image size was at least 128 x 128. I chose to use a basis image size of 256 x 256.

Each type of sand paper tended to have a characteristic shape. The following image shows the characteristic shape for each of the four types of sandpaper that were sampled.

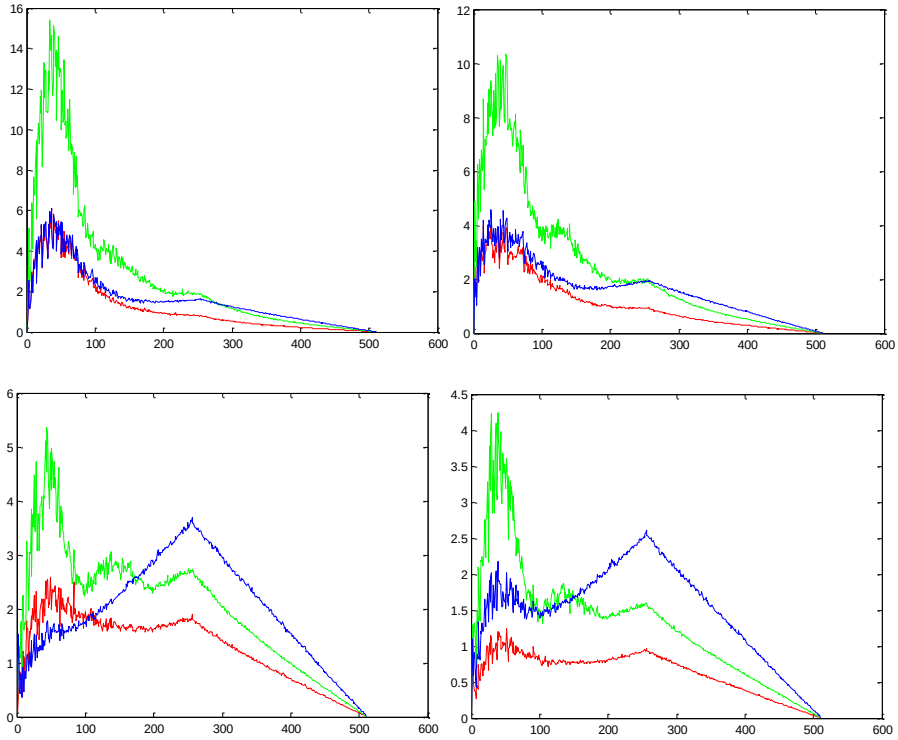

FIGURE 10 - CHARACTERISTIC PLOTS FOR 40 GRIT, 50 GRIT, 80 GRIT, AND 120 GRIT SANDPAPER

DC BASIS IMAGE NORMALIZATION

The exposure time of the samples was not consistent. The reflectance magnitude was correspondingly higher for images that were exposed for a longer period of time. In order to correct the exposure differences between the images, the contribution of each basis image was divided by the magnitude of the DC basis image.

CALCULATIONS BASED ON DCT DIAGONALS

In order to quantitatively compare the DCT diagonals data for different samples, the Euclidian distance between a basis sample and a comparison sample was calculated for each diagonal. The distances were summed for each of the color spectrums. The following table details the results.

Basis Sample	Test Sample	Red Distance	Green Distance	Blue Distance
2 at (90, 90)	2 at (110, 110)	10.2	-10.7	14.0
2 at (90, 90)	3 at (90, 90)	183.4	489.7	156.0
2 at (90, 90)	3 at (110, 110)	199.2	521.1	176.3

3 at (90, 90)	3 at (110, 110)	15.7	31.4	20.2
5 at (90, 90)	5 at (110, 110)	0.9	-0.2	2.7
5 at (90, 90)	6 at (90, 90)	-21.4	-39.1	-88.6
5 at (90, 90)	6 at (110,110)	-17.5	-43.0	-88.0
6 at (90, 90)	6 at (110, 110)	3.9	-4.9	0.8
8 at (90, 90)	8 at (110, 110)	9.3	2.2	9.6
8 at (90, 90)	9 at (90, 90)	-20.0	18.0	-55.8
8 at (90, 90)	9 at (110, 110)	-15.9	25.3	-48.8
9 at (90, 90)	9 at (110, 110)	4.0	7.3	7.0
10 at (90, 90)	10 at (110, 110)	2.6	5.8	7.0
10 at (90, 90)	11 at (90, 90)	-19.3	-23.0	-69.6
10 at (90, 90)	11 at (110, 110)	-17.5	-23.0	-66.4
10 at (90, 90)	12 at (90, 90)	-23.2	-37.6	-104.6
10 at (90, 90)	12 at (110, 110)	-21.8	-38.3	-100.6

The following chart shows the sum of the absolute value of the distances.

Basis Sample	Test Sample	Red Distance	Green Distance	Blue Distance
2 at (90, 90)	2 at (110, 110)	59	130	59
2 at (90, 90)	3 at (90, 90)	198	497	214
2 at (90, 90)	3 at (110, 110)	213	528	230
3 at (90, 90)	3 at (110, 110)	34	79	40
5 at (90, 90)	5 at (110, 110)	40	101	46
5 at (90, 90)	6 at (90, 90)	63	140	113
5 at (90, 90)	6 at (110,110)	59	142	111
6 at (90, 90)	6 at (110, 110)	41	104	52
8 at (90, 90)	8 at (110, 110)	35	55	25
8 at (90, 90)	9 at (90, 90)	68	92	79
8 at (90, 90)	9 at (110, 110)	71	95	73
9 at (90, 90)	9 at (110, 110)	31	47	21
10 at (90, 90)	10 at (110, 110)	13	38	23
10 at (90, 90)	11 at (90, 90)	30	61	83
10 at (90, 90)	11 at (110, 110)	31	62	82
10 at (90, 90)	12 at (90, 90)	35	67	133
10 at (90, 90)	12 at (110, 110)	35	65	108

In order to verify that the algorithm works for the 120 wavelength spectrum, the following data was calculated using a sum of the absolute difference for each of the wavelengths.

Basis Sample	Test Sample	Spectrum Sum
2 at (90, 90)	2 at (120, 120)	290

2 at (90, 90)	3 at (90, 90)	932
2 at (90, 90)	3 at (120, 120)	1007
3 at (90, 90)	3 at (120, 120)	205
5 at (90, 90)	5 at (120, 120)	250
5 at (90, 90)	6 at (90, 90)	356
5 at (90, 90)	6 at (120,120)	363
6 at (90, 90)	6 at (120, 120)	262
8 at (90, 90)	8 at (120, 120)	201
8 at (90, 90)	9 at (90, 90)	300
8 at (90, 90)	9 at (120, 120)	299
9 at (90, 90)	9 at (120, 120)	203
10 at (90, 90)	10 at (120, 120)	138
10 at (90, 90)	11 at (90, 90)	206
10 at (90, 90)	11 at (120, 120)	195
10 at (90, 90)	12 at (90, 90)	238
10 at (90, 90)	12 at (120, 120)	240

FFT PHASE ANGLE DESCRIPTION OF PLOT SHAPE

An attempt was made to use the phase of the FFT of the diagonal plots to describe the shape of the plot. If the technique was successful, the magnitude of the reflectance in the image would not be a factor in the measurement of the plot. However, the FFT phase results did not consistently provide meaningful results. The following image shows the FFT phase plot of two areas of sample 10 as well as the DCT diagonal plots for the areas.

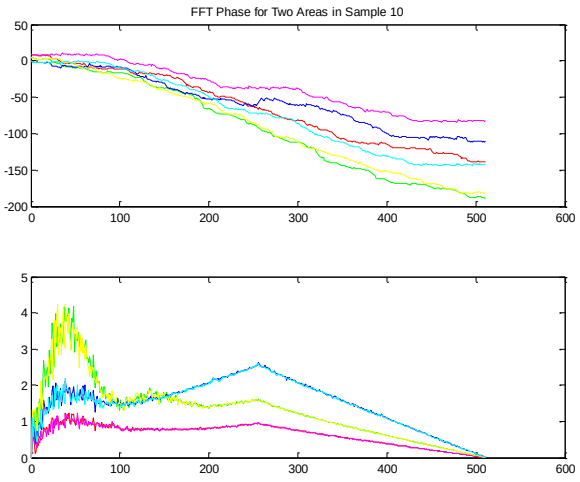

FIGURE 11 – FFT PHASE ANGLE SHAPE DESCRIPTION PLOT

DIRECT COSINE TRANSFORMATION CONCLUSIONS

Difference calculations for images selected from the same sample were much smaller than the differences between images from two different samples. Sample 11 is more similar to sample 10 than sample 12 is to sample 10 which is what was expected. The results were repeatable across different areas of the sandpaper samples.

The Direct Cosine Transformation Diagonals may provide a reliable means to verify that a sandpaper sample is close to an established standard. The impact of the magnitude of reflectance was removed by dividing the results by the contribution of the DC basis image.

Attempts to measure the shape of the DCT diagonal plots with the FFT phase were unsuccessful.

CHAPTER 4 - RX DETECTOR ALGORITHM

The RX algorithm originally developed by Reed and Yu (1990) was designed to detect anomalies in an image. The RX detector algorithm extracts targets that are spectrally distinct from their surroundings. For each pixel vector **r**, the RX detector calculates the Mahalanobis distance given by:

$$\delta_{RXD}(r) = (r-\mu)^T K_{LxL}^{-1}(r-\mu) \text{ EQUATION 1}$$

Where μ is the sample mean and K_{LxL} is the covariance matrix. Anomalies in the data will be specified by small eigenvalues. A small eigenvalue will produce a large value for δ_{RXD}.

RXD SAMPLE TESTING METHODOLOGY

A covariance matrix will be created from a known good sample. The distance from the covariance matrix will be calculated for each pixel vector of a sample to be tested. Statistical methods will be used to analyze the pixel distances and determine the degree of variation from the known good sample.

A covariance matrix was formed from a large portion of one of the images of each sample type. Following is the covariance matrix formed from sample 2 and the resulting RXD distance image for an area of sample 2.

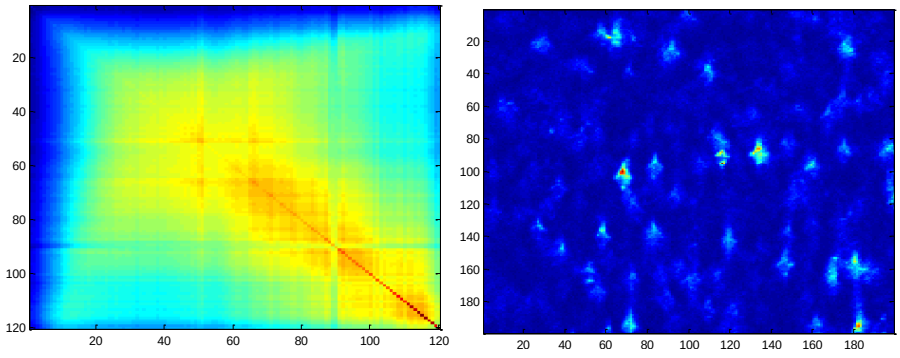

FIGURE 12- COVARIANCE MATRIX AND RXD IMAGE OF SAMPLE 2

Four 100 X 100 pixel sample areas from each image were compared to the covariance matrix. The standard deviation for the pixel distances was calculated for each sample area. The following tables contain the standard deviation calculation results.

Standard Deviation for 50 Grit AO, Samples 2 and 3, Using Covariance Matrix from Sample 2			
Sample 2 Grit Weight – 1.672 grams		Sample 3 Grit Weight – 1.875 grams	
Area 1	36.8	Area 1	15.2
Area 2	45.9	Area 2	18.4
Area 3	41.7	Area 3	16.0
Area 4	46.2	Area 4	19.0

Standard Deviation for 40 Grit AO, Samples 5 and 6, Using Covariance Matrix from Sample 5			
Sample 5 Grit Weight – 2.5199 grams		Sample 6 Grit Weight – 3.4255 grams	
Area 1	45.7	Area 1	27.9
Area 2	33.1	Area 2	23.0
Area 3	27.9	Area 3	19.4
Area 4	29.4	Area 4	24.4

Standard Deviation for 80 Grit AO, Samples 8 and 9, Using Covariance Matrix from Sample 8			
Sample 8 Grit Weight – 1.31 grams		Sample 9 Grit Weight – 1.844 grams	
Area 1	18.6	Area 1	17.1
Area 2	18.2	Area 2	16.5
Area 3	20.1	Area 3	15.2
Area 4	21.0	Area 4	15.1

Standard Deviation for 120 Grit ZO, Samples 10, 11 and 12, Using Covariance Matrix from Sample10					
Sample 10 – 0.573 grams		Sample 11 – 0.883 grams		Sample 12 – 1.103 grams	
Area 1	16.4	Area 1	15.2	Area 1	14.2
Area 2	16.8	Area 2	15.6	Area 2	14.7
Area 3	16.3	Area 3	14.7	Area 3	14.2
Area 4	16.1	Area 4	14.7	Area 4	14.3

STATISTICAL METHODS ANALYSIS RESULTS

In theory, the sample areas from the covariance matrix image should have a lower standard deviation than sample areas from other images. The standard deviation results in the previous table do not support this hypothesis. The results consistently indicate that the standard deviation is lower for higher grit density samples. Changing the source image for the covariance matrix does not significantly alter the results.

In order to better understand the RXD results. The top image is a representation of the frequency of a certain pixel type in an image. The bottom image represents the magnitude of each pixel.

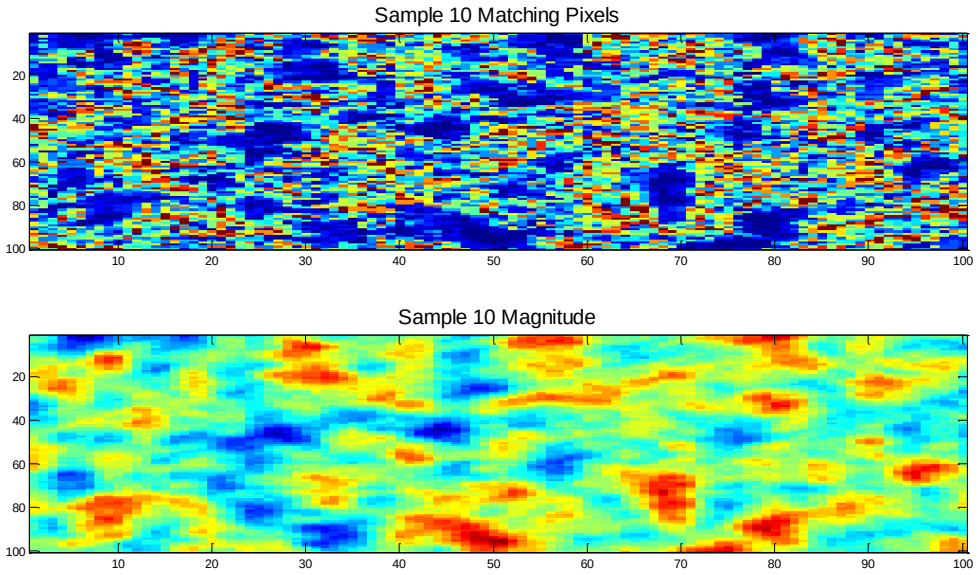

FIGURE 13- PIXEL VECTOR OCCURANCE FREQUENCY AND IMAGE REFLECTANCE

The areas of high grit concentration are represented by the blue areas in the lower image. The areas of high glue concentration are represented by the red areas in the lower image. The mixed pixels are represented by the bluish green areas. The dark blue areas in the top image represent areas that contain pixels that do not occur very often in the image. The red pixels indicate areas that occur frequently in the image. The vast majority of pixels are mixed pixels of glue and grit.

In the 40 grit and 50 grit samples, there are large glue only areas. This glue only area increased the standard deviation of the RXD results. The higher grit density samples closed up some of the glue areas to create a more uniform mixed pixel image that had a correspondingly lower standard deviation.

The 80 grit and 120 grit samples displayed the same behavior as the 40 grit and 50 grit samples. However, the amount of open glue areas in the 80 grit and 120 grit samples are much more limited. Hence the change in standard deviation was much smaller for those samples.

EXPERIMENTS WITH TAILORED COVARIANCE MATRIX

Rather than using a covariance matrix that represented the entire sample, a tailored covariance matrix might make certain areas of the image more visible. Based on the previous testing, three logical choices exist for designing tailored covariance matrices. The covariance matrix could be created from a homogeneous collection of grit pixels, glue pixels, or mixed pixels.

The methods used to create homogeneous images for each of the covariance types was similar. For the grit homogeneous image, several samples with in a tolerance of the lowest energy sample were collected and placed in an image. For the glue homogeneous image, a percentage of the highest energy pixels were collected and placed in an image. The mixed pixel image was created by finding the pixels that appeared most often. All the bands of each pixel were summed to form a single magnitude for each pixel. The number of times that magnitude occurred in the image was calculated for each pixel. The following is an example of the matching pixels sums for a small 10x10 image.

4	2	1	2	2	2	1	4	3	3
4	4	3	2	1	3	2	4	3	1
3	1	1	1	1	2	2	2	1	3
4	2	1	3	1	1	3	3	1	1
7	2	4	1	4	4	2	1	2	1
2	7	4	1	3	5	3	2	1	3
2	5	7	3	7	1	2	2	3	1
7	5	5	3	3	1	1	3	3	3
4	7	3	7	5	1	2	1	3	2
4	3	3	3	3	3	1	1	1	1

The pixels with 7 matching pixels would be chosen to populate the homogeneous mixed grit-glue image. The following image was created to verify that the pixels chosen for the homogeneous image contain similar spectrums.

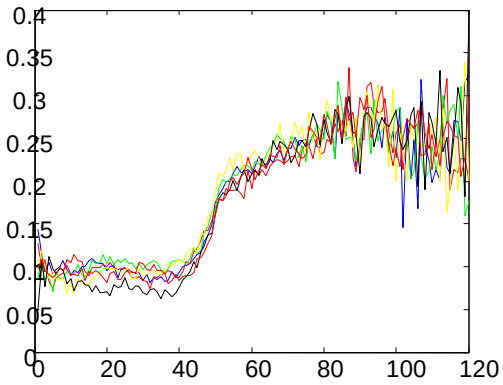

FIGURE 14 – MOST COMMON PIXELS MATCHING SPECTRUM

TAILORED COVARIANCE MATRIX RESULTS

The following images display typical RXD algorithm results for a grit tailored covariance matrix and a glue tailored covariance matrix.

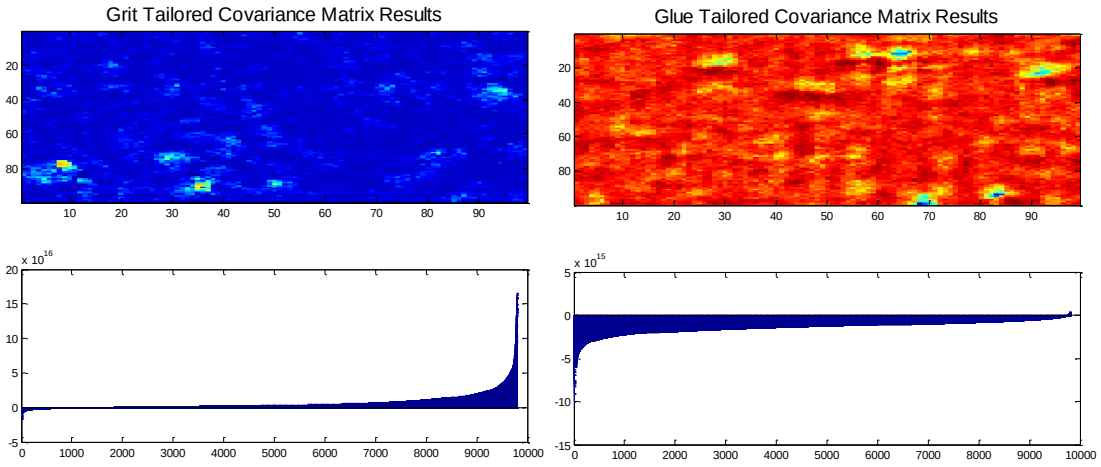

FIGURE 15 – GRIT TAILORED AND GLUE TAILORED COVARIANCE MATRIX RESULTS

If only a small number of pixels were used, the covariance matrix would typically contain values along the main diagonal that were extremely small. The small values would be inverted during the RXD calculation. The RXD image could contain values greater than 10 raised to the 16th power.

The grit and glue tailored covariance matrix images did not seem to present a convergent means to determine grit density.

If the covariance matrix was constructed from a small number of the most common pixel vectors, the resulting RXD distances were split in to positive and negative distances. An attempt was made to use the number of positive and negative distances as a means to indicate the proportions of grit coverage. Samples 5 and 6 as well as samples 10, 11, and 12 produced results that indicated potential for the algorithm. However, samples 2 and 3 as well as samples 8 and 9 did not produce positive results. The following image shows the results for a covariance matrix generated from a small sample of common pixels from sample 10.

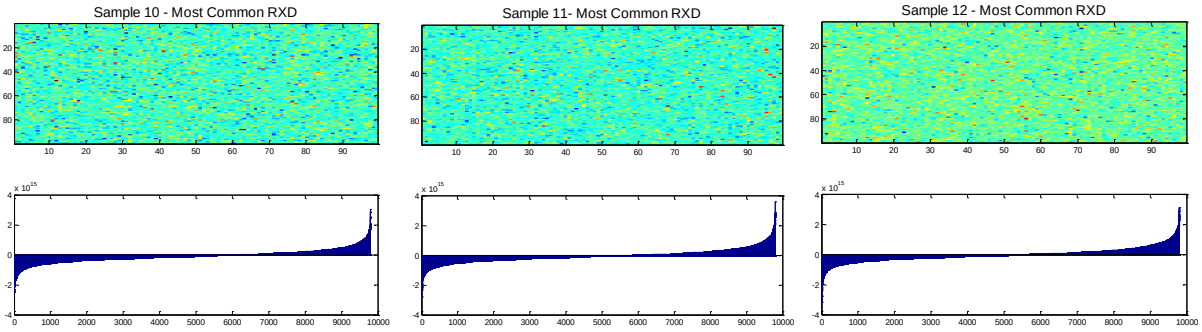

FIGURE 16 – MOST COMMON PIXEL TAILORED COVARIANCE MATRIX RESULTS

CONCLUSIONS FROM RXD RESULTS

The standard deviation for the RXD images was consistently lower for images with more grit than images with less grit. The glue areas were found to be more spectrally diverse than grit areas. The high diversity of the glue areas increased the standard deviation of the RXD image. The spectral diversity of the glue areas may be due to variations caused by several factors including the backing material, the thickness of the glue, small grit particles and glare caused by the light source. Also, most pixel vectors contained a combination of glue and grit. As the grit density increased, the image became more uniform because fewer glue only areas remained. The standard deviation of the RX detector algorithm showed potential to provide an indication of the variation of grit application compared to a known standard.

Attempts to use a tailored grit or glue covariance matrix did not produce results that lead to a means of characterizing grit density. The most common pixel tailored covariance matrix seemed to provide a possible solution by totaling positive and negative distances of the RX detector algorithm. However, the results were not consistent across all of the sandpaper samples.

CHAPTER 5 - LINEAR SPECTRAL MIXTURE ANALYSIS APPROACHES TO DETERMINE SANDPAPER GRIT DENSITY

LINEAR MIXTURE BACKGROUND AND APPROACHES

Each **pixel vector (r)** of a hyperspectral sandpaper image is assumed to contain a linear spectral mixture of the ingredients in the sandpaper. The spectral signatures of the elements in the sandpaper form a **signature matrix ($M = m_1, m_2, ..., m_p$)**. The amount that any one spectral signature of the signature matrix contributes to the spectrum of an individual pixel vector is given by an **abundance fraction ($\alpha = \alpha_1, \alpha_2, ..., \alpha_p$)**.

$$R = M\alpha + n \quad \text{EQUATION 2}$$

Where **n** is noise.

If the signature matrix and the abundance fractions can be determined accurately, the density of grit on the sandpaper could be calculated.

TWO MOST DIVERGENT PIXELS SIGNATURE MATRIX ALGORITHM

One would expect two main ingredients, glue and grit, to constitute the signature matrix of sandpaper. Pixels that are primarily glue should be maximally divergent from the pixels that are primarily grit.

Based on an assumption that the sandpaper is made from two basic elements, glue and grit, an algorithm will be explored that uses the two most divergent pixels in the image to form two target signature vectors that make up the signature matrix. Two methods will be used to calculate the abundance fractions.

The first abundance fraction calculation method will use an **unconstrained** least-squares estimate developed by Scharf, 1992.

The second abundance fraction calculation method will use an assumption that the abundance fractions should be the same for all wavelengths. Based on this assumption it should be possible to

solve 2 equations for 2 unknowns. The 2 unknowns will be the two abundance fractions that represent the percentage of glue and grit in the sand paper.

UNSUPERVISED FULLY CONSTRAINED LEAST SQUARES ALGORITHM

In reality, the spectrums of the areas of sandpaper that are primarily glue are influenced by the type of backing, paper or cloth, and the thickness of the glue. The grit is typically a mixture of various colors of Aluminum Oxide. Also, grit is not limited to aluminum oxide. Sometimes for example the grit may include a combination of garnet, aluminum oxide and some contaminants. An unsupervised algorithm to generate the signature matrix will be explored that allows for the automatic generation of a multitude of signature vectors.

Intuitively, the sum of the abundance fractions should equal one, if the signature matrix includes all of the possible spectral components of the sandpaper. Also, all of the abundance fractions should be positive because it is physically impossible to have a negative proportion of any of the signature vectors. A "fully constrained" algorithm developed by Chang that imposes these two constraints on the linear unmixing process will be explored.

ABUNDANCE FRACTION ESTIMATE UTILIZING TWO MOST DIVERGENT PIXELS IN SIGNATURE MATRIX

DETERMINATION OF MOST DIVERGENT PIXELS

The two most divergent pixel vectors will be located finding the pixels with the greatest Jeffries-Matusita Distance (JMD). The JMD formula is as follows:

$$JMD(r_i,r_j) = \sqrt{\sum_{l=1}^{L}\left[\sqrt{p_l} - \sqrt{q_l}\right]^2} \quad \text{EQUATION 3}$$

Where p and q are hyperspectral reflectances of pixel vectors r_i and r_j.

Originally an algorithm that calculated the JMD for every pixel vector pair combination was implemented. The pixel vector pair with the greatest JMD was chosen as the most divergent pixels. This algorithm was impractically slow for image sizes of more than a couple hundred pixels.

Alternatively, the pixel vector with the highest JMD when compared to the pixel vector at x=1, y=1 was chosen as the first divergent pixel. Then the other divergent pixel was found by calculating the JMD across the image with r_i equal to the first divergent pixel. This required only two passes through the data. The shorter search algorithm was tested and verified.

The following table lists the most divergent pixels and the JMD for each of the sandpaper samples.

Sample	Description	Most Divergent Pixels	JMD
2	50 Grit on Paper, AO with Urea, 1.67 gm	(39, 21) and (33, 27)	5.35
3	50 Grit on Paper, AO with Urea, 1.86 gm	(28, 4) and (40, 32)	3.41
5	40 Grit on Paper, AO with Urea, 2.52 gm	(40, 2) and (1, 3)	4.67
6	40 Grit on Paper, AO with Urea, 3.43 gm	(19, 13) and (19, 29)	5.26
8	80 Grit on Cloth, AO with Phenolic, 1.31 gm	(19, 6) and (7, 37)	1.24
9	80 Grit on Cloth, AO with Phenolic, 1.84 gm	(38, 19) and (25, 9)	1.06
10	120 Grit on Paper, Z and AO with Phenolic, .573 gm	(3, 24) and (28, 20)	1.49
11	120 Grit on Paper, Z and AO with Phenolic, .883 gm	(37, 29) and (9, 5)	1.79
12	120 Grit on Paper, Z and AO with Phenolic, 1.1 gm	(9, 14) and (10, 1)	1.29

The JMD for samples 2, 3, 5, and 6 are large in comparison to the other samples. These samples are comprised of a black aluminum oxide on light color glue. The contrast between the grit and glue is significant and the JMD is correspondingly large. Samples 8 and 9 are red aluminum oxide on red glue. The contrast between the grit and glue is small and the JMD is low. Samples 10, 11, and 12 are the finest grit samples. The fine grit covers the glue and backing such that no significantly large glue area as compared to the size of the camera pixel is left exposed. Hence, all pixels are mixed pixels of glue and grit. The resulting JMD is relatively low for these somewhat uniform images. Sample 11 is a little overexposed compared to samples 10 and 12.

The following image displays the spectrum for the two most divergent pixels from sample 12. The red line indicates a mostly glue pixel spectrum and the blue line indicates a mostly grit pixel spectrum.

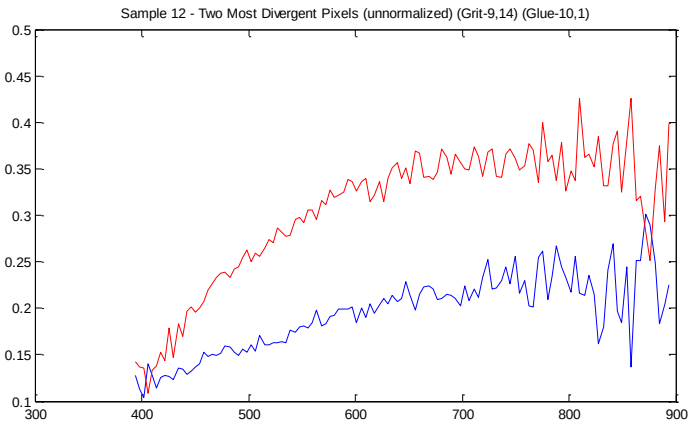

FIGURE 17- TWO MOST DIVERGENT PIXEL VECTORS FOR SAMPLE 12

The pixel vectors of the two most divergent pixels calculated above are assumed to be pixels of pure grit and pure glue. The spectrum of those two pixel vectors forms the basis spectrum.

$$M = [r_1, r_2] \text{ EQUATION 4}$$

The abundance fractions that solve $\mathbf{r = M\alpha + n}$ will be determined by Scharf's unconstrained least squares estimate and a two equation and two unknowns approach.

UNCONSTRAINED LEAST SQUARES ESTIMATE

The least-squares estimate of $\boldsymbol{\alpha=(\alpha_1\ \alpha_2\ \ldots\ \alpha_p)^T}$ for $\mathbf{r = M\alpha + n}$ denoted by $\boldsymbol{\alpha_{LS}}$ can be obtained by: **(Scharf, 1992)**

$$\boldsymbol{\alpha_{LS} = (M^TM)^{-1}M^Tr} \text{ EQUATION 5}$$

Where **M** is the signature matrix and **r** is a hyperspectral pixel vector. The signature matrix only contains two elements. Therefore only two abundance fractions will be obtained. One abundance fraction should represent the portion of the pixel that is comprised of grit and the other abundance should represent the portion of the pixel that is comprised of glue. If the abundance fractions are averaged over a significant number of pixels, a value that represents the density of grit application can be obtained.

The following table shows the average abundance fractions for a 40 pixel by 40 pixel region of each sample.

Sample	Grams/In^2	LSE Grit	LSE Glue	Sum Glue and Grit
2	.105	.296	.760	1.06
3	.117	.388	.534	.922
5	.158	.254	.928	1.18
6	.215	.217	1.30	1.52
8	.082	.370	.660	1.03
9	.116	.465	.478	.943
10	.036	.539	.443	.982
11	.055	.534	.420	.954
12	.069	.465	.517	.982

The least squares error calculation does not consistently produce results that align with the sample grit weights. The glue contribution to sample #6 was calculated as a nonsensical 130%. Clearly, the **unconstrained** least squares solution is not acceptable.

TWO EQUATIONS AND TWO UNKNOWNS ALGORITHM

Another approach to obtaining the abundance fractions would be to solve two linear equations with two unknowns. If the basic assumption that sandpaper can be described with a basis matrix of only two elements is accurate, then the ratio of those two elements present in any pixel should be consistent across all of the wavelengths of the pixel vector. The assumption that abundance fractions are consistent across all wavelengths combined with an assumption that the sum of the ratios is equal to one allows the linear unmixing problem to become a simple case of two equations with two unknowns.

$$r = m_1\alpha_1 + m_2\alpha_2 \quad \text{EQUATION 6}$$

$$\alpha_{1+}\,\alpha_2 = 1 \quad \text{EQUATION 7}$$

Where $\mathbf{m_1}$ is the signature spectrum of grit, $\boldsymbol{\alpha_1}$ is the abundance fraction for grit, $\mathbf{m_2}$ is the signature spectrum of glue, and $\boldsymbol{\alpha_2}$ is the abundance fraction for glue.

In reality, it is not the case that all wavelengths are satisfied by the same abundance fractions. The bands in the blue and green spectrums tended to have fairly consistent abundance fractions. The longer wavelength red spectrum bands tended to have the highest variation in abundance fractions and often included negative values. However, averaging or taking the median value for the abundance fractions provided reasonable results.

The following chart shows the values calculated for average and median grit values with a measure of the variance in abundance fractions.

Sample	Grams/In²	Ave Grit	Median Grit	Variance
2	.105	.657	.673	.019
3	.117	.656	.668	.022
5	.158	.623	.664	.029
6	.215	.626	.652	.016
8	.082	.486	.569	.091
9	.116	.535	.603	.082
10	.036	.455	.461	.038
11	.055	.491	.529	.036
12	.069	.516	.578	.066

The following chart shows the same calculations with the equations reversed to calculate average and median values for the glue abundance fraction.

Sample	Grams/In²	Ave Glue	Median Glue	Variance
2	.105	.325	.323	.010
3	.117	.321	.328	.009
5	.158	.344	.325	.02
6	.215	.360	.342	.016
8	.082	.340	.316	.066
9	.116	.343	.332	.054
10	.036	.483	.517	.042
11	.055	.449	.452	.037
12	.069	.376	.375	.048

DOWN SAMPLED BANDS

The effect of down sampling the number of bands was explored. The following data was generated by averaging 4 bands at a time to create a 30 band image.

Sample	Grams/In²	Ave Grit	Median Grit	Variance
2	.105	.661	.671	.010
3	.117	.662	.668	.009
5	.158	.628	.662	.02
6	.215	.627	.649	.016
8	.082	.504	.583	.066
9	.116	.568	.624	.054
10	.036	.471	.468	.042
11	.055	.502	.530	.037
12	.069	.513	.580	.048

MOST DIVERGENT LINEAR UNMIXING RESULTS

The results of the two equations and two unknowns algorithm look good for the red samples 8 and 9 as well as the brown samples 10, 11, and 12. The samples with the largest JMD actually produce results that do not correlate well. However the images of samples 2 and 5 have a noticeable glare on some of the glue pixels. The increased glare moves the glue basis matrix higher in the reflectance spectrum than it should be. A larger ratio of the grit basis pixel vector

is required to offset the elevated glue basis pixel vector in samples 2 and 5. The RGB converted image of sample 2 shows some of the glare produced by the reflection of the sun.

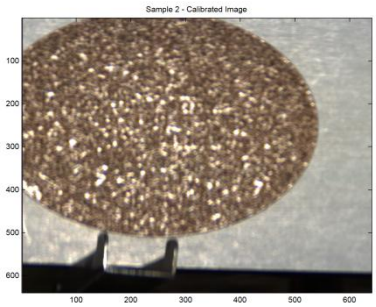

FIGURE 18- GLARE IN SAMPLE 2 RGB CONVERTED IMAGE

The abundance fractions selected by the median look to be more accurate than the abundance fractions generated by an average function. The average abundance fractions may be skewed due to the high variance in abundance ratios of the longer wavelength bands.

The abundance fraction ratios seem to correspond with the measured grit density. However, the magnitude of change in the abundance fractions is much lower than what would be expected. The camera was positioned at a slight angle to the sandpaper. The angle increases the portion of the sandpaper that is covered by grit.

The variance measurement was an attempt to characterize how well the linear combination of the basis pixels described the pixels. The images with the smaller difference between the glue pixel and the grit pixel contained the highest variation indicating that the pixels were not as accurately described by the linear combination of the basis pixel vectors.

The down sampled 30 band image produced very similar results to the 120 band image.

UNSUPERVISED MODIFIED FULLY CONSTRAINED LEAST SQUARES ALGORITHM

UNSUPERVISED SIGNATURE MATRIX GENERATION PROCESS

Chang describes an unsupervised signature matrix generation process that is similar to the most divergent pixels approach that was previously explored. Chang suggest selecting the highest energy pixel vector by finding the pixel vector r that satisfies:

$$m_0 = \text{ARG}\{max_r[r^T r]\} \quad \text{EQUATION 8}$$

The second pixel vector in the signature matrix is determined by finding the pixel vector that satisfies the following equation:

$$m_1 = \text{ARG}\{max_r[(r - m_0)^T (r - m_0)]\} \quad \text{EQUATION 9}$$

More pixel vectors are iteratively added to the signature matrix if there is a pixel in the image that is not accurately described by a linear combination of the current signature matrix. In other words, if the least squares error as calculated by the following equation is greater than a threshold ϵ, then the pixel with the highest least squares error is added to the signature matrix.

$$LSE^{(k)}(r) = (r - \left[\sum_{i=0}^{k} \hat{a}_i^{(k)}(r) m_i\right])^T (r - \left[\sum_{i=0}^{k} \hat{a}_i^{(k)}(r) m_i\right]) \quad \text{EQUATION 10}$$

I chose to modify Chang's algorithm slightly. Rather than selecting the highest energy pixel, I chose the lowest energy pixel. The lowest energy pixel is typically a pixel that is entirely or mostly composed of grit.

ABUNDANCE FRACTION CALCULATION

A fully constrained least squares approach will be explored for determination of the abundance fractions. The abundance fractions will be constrained to be all non-negative and they must sum to one.

$$\boldsymbol{\alpha_J \geq 0 \text{ for all } 1 \leq J \leq p, \text{ and } \sum \alpha_J = 1} \quad \text{EQUATION 11}$$

ABUNDANCE FRACTION SUM TO ONE CONSTRAINT

In Chang's Modified Fully Constrained Least Squares abundance fraction calculation algorithm, the sum to one constraint is applied first. Then a Lagrange multiplier technique is utilized to apply the non-negative abundance fraction constraint.

Imposing the sum to one constraint on equation 2-1 produces the following linear mixing problem:

$$\mathbf{min}_{\alpha\epsilon\Delta}\{(\mathbf{r}-\mathbf{M}\alpha)^T(\mathbf{r}-\mathbf{M}\alpha)\}\ \mathbf{subject\ to}\ \Delta\{\alpha \mid \sum^p \alpha_j = 1\} \qquad \text{EQUATION 12}$$

The sum to one constrained least-squares solution derived by **(Chang 2003)** utilizes an orthogonal subspace projection (OSP) technique. The orthogonal subspace projector $P_{M,1}^{\perp}$maps the least squares abundance fractions calculated using Equation 5 in to the space orthogonal to <M,1>. The sum to one constrained least squares solution derived by Chang is given by the following:

$$\alpha_{SCLS} = P_{M,1}^{\perp}\alpha_{LS}(\mathbf{r}) + (\mathbf{M}^T\mathbf{M})^{-1}\mathbf{1}[\mathbf{1}^T(\mathbf{M}^T\mathbf{M})^{-1}\mathbf{1}]^{-1} \qquad \text{EQUATION 13}$$

Where the orthogonal projection $P_{M,1}^{\perp}$ is given by

$$P_{M,1}^{\perp} = \mathbf{I}_{LXL} - (\mathbf{M}^T\mathbf{M})^{-1}\mathbf{1}[\mathbf{1}^T(\mathbf{M}^T\mathbf{M})^{-1}\mathbf{1}]^{-1}\mathbf{1}^T \qquad \text{EQUATION 14}$$

with $\mathbf{1}$ = (1 1 … 1)^T being a p-dimensional column vector.

NONNEGATIVE ABUNDANCE FRACTION CONSTRAINT

Imposing the nonnegative constraint on the abundance fractions yields the following optimization problem:

$$\mathbf{Minimize\ LSE} = (\mathbf{M}\alpha - \mathbf{r})^T(\mathbf{M}\alpha-\mathbf{r})\ \mathbf{subject\ to}\ \alpha \geq \mathbf{0} \qquad \text{EQUATION 15}$$

Chang solves the non-negative constraint problem by applying the sum to one constraint and the absolute abundance sum to one constraint at the same time to create an equation that can be solved with a Lagrange multiplier method. In other words, the solution to the fully constrained abundance fraction is given by:

$$min_{\alpha\epsilon\Delta_f}\{(r - M\alpha)(r - M\alpha)^T\} \qquad \text{EQUATION 16}$$

Subject to

$$\Delta = \{\alpha|\sum_{j=1}^{P}\alpha_j = 1\ and \sum_{j=1}^{P}|\alpha_j| = 1\} \qquad \text{EQUATION 17}$$

The resulting Lagrange multiplier equation created from the Equations 16 and 17 is given by:

$$J(\alpha) = \left(\frac{1}{2}\right)(r - M\alpha)(r - M\alpha)^T - \lambda_1\left(\sum_{j=1}^{P}\alpha_j - 1\right) - \lambda_2\left(\sum_{j=1}^{P}|\alpha_j| - 1\right) \text{EQUATION 18}$$

The following equation for the Modified Fully Constrained Least Squares Abundance Fractions can be derived, after differentiating equation 18 with respect to α and setting the result equal to zero.

$$\hat{\alpha}_{MCLS} = \hat{\alpha}_{SCLS} - (M^T M)^{-1}[\lambda_1 \mathbf{1} - \lambda_2 sign(\alpha)] \qquad \text{EQUATION 19}$$

If $\hat{\alpha}_{SCLS}$ is substituted for α in Equation 19, then the following two equations can be used to solve for $\lambda_1$and λ_2.

$$\sum_{j=1}^{P} \alpha_j = \mathbf{1}^T \alpha = 1 \qquad \text{EQUATION 20}$$

$$\sum_{j=1}^{P} |\alpha_j| = sign(\alpha)^T \alpha = 1 \qquad \text{EQUATION 21}$$

Iteratively computing λ_1, λ_2, and $\hat{\alpha}_{MCLS}$ using Equations 19, 20, and 21 can obtain a solution to Equations 16 and 17.

The process of calculating the abundance fractions utilizing the Modified Fully Constrained Least Squares approach derived by Chang can be summarized as follows.

1. Calculate a set of sum to one constrained abundance fractions (α_{SCLS}) using Equation 13.
2. If all of the abundance fractions are positive, then $\alpha_{MCLS} = \alpha_{SCLS}$
3. If any of the abundance fractions are negative, then utilize $\hat{\alpha}_{SCLS}$ in Equation 19 and solve for λ_1 and λ_2 by plugging the follow equation for λ_1

$$\lambda_1 = -\lambda_2((M^T M)^{-1} sign(\alpha_{SCLS}))/((M^T M)^{-1}\mathbf{1}) \qquad \text{EQUATION 22}$$

in to the following summation and solving for λ_2.

$$\sum_{j=1}^{P} abs(\alpha_1 - (M^T M)^{-1}[\lambda_1 - \lambda_2 sign(\alpha_1)]) + \cdots + abs((\alpha_1 - (M^T M)^{-1}[\lambda_1 - \lambda_2 sign(\alpha_1)]) = 1 \qquad \text{EQUATION 23}$$

4. Utilize λ_1 and λ_2 and Equation 19 to calculate $\hat{\alpha}_{MCLS}$.
5. If all of the abundance fractions in $\hat{\alpha}_{MCLS}$ are positive then$\alpha_{MCLS} = \hat{\alpha}_{MCLS}$.
6. If some of the abundance fractions are negative, then set $\hat{\alpha}_{SCLS} = \hat{\alpha}_{MCLS}$ and go back to step 3.

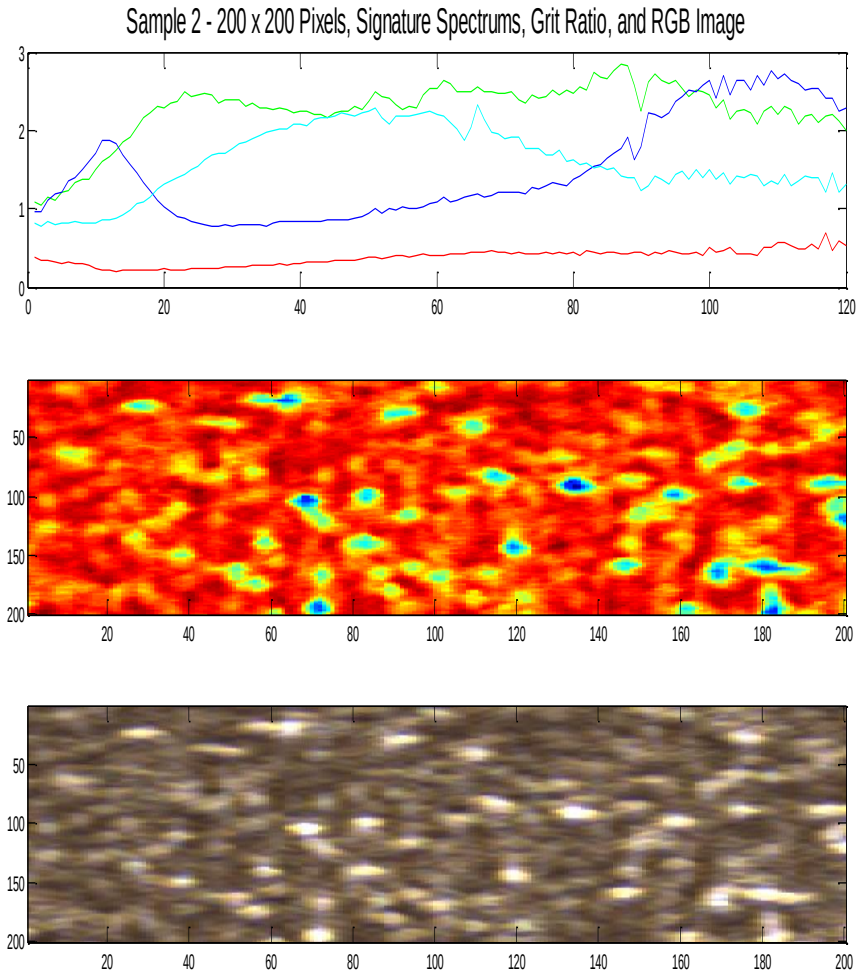

FIGURE 19- SAMPLE 2 – 200X200 PIXELS, SIGNATURE SPECTRUM, GRIT RATIO, AND RGB IMAGE

Sample 2							
Location and Size	Grit Ratio	Ratio 2	Ratio 3	Ratio4	Error	Negs	Starting Ratio
(100, 100) – 100x100	.7705	.0828	.1183	.0284	1.002	1720-174	.7804,.0923,.1155,.012
(100, 200) – 100x100	.8116	.1639	.0033	.0212	1.087	5470-3468	.8153,.165,.0082,.0115
(200, 100) – 100x100	.7091	.0631	.1191	.1087	1.143	865-148	.713,.0668,.1155,.1047
(200, 200) – 100x100	.7327	.0270	.0716	.0988	1.104	2027-336	.7353,.0873,.0595,.118
(100, 100) – 200x200	.7605	.0894	.0880	.0621	1.107	3890-240	.7657,.098,.0839,.0523

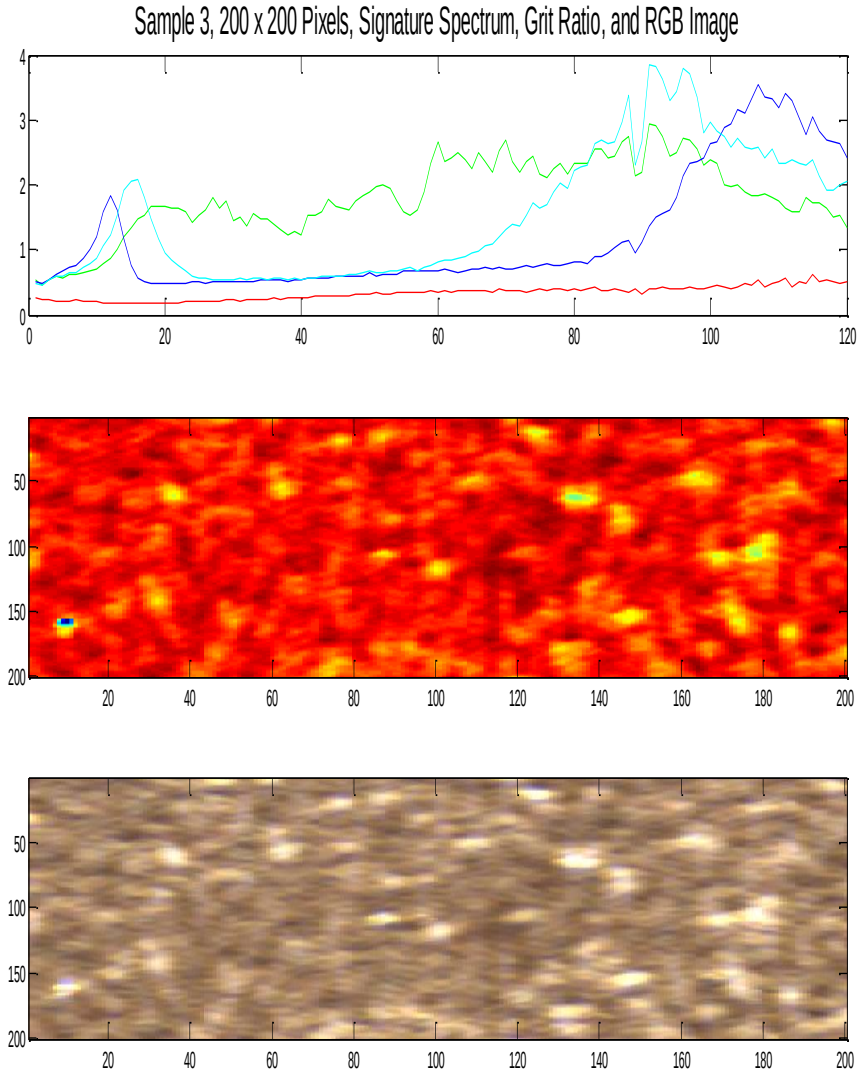

FIGURE 20-SAMPLE 3, 200X200 PIXEL, SIGNATURE SPECTRUM, GRIT RATIO, AND RGB IMAGE

Sample 3							
Location and Size	Grit Ratio	Ratio 2	Ratio 3	Ratio4	Error	Negs	Starting Ratio
(100, 100) – 100x100	.6282	.2747	.0971		.7595	3164-0	.6607,.2999,.0394
(100, 200) – 100x100	.6755	.1885	.0891	.0469	.6236	7358-277	.7156,.2718,.0437,-.031
(200, 100) – 100x100	.878	.0945	.0346	-.0019	.9534	896-143	.8714,.1017,.0578,-.016
(200, 200) – 100x100	.6343	.1539	.2119		.6748	499-0	.6332,.1506,.2162
(100, 100) – 200x200	.8524	.1195	.028	.0001	1.087	3714-934	.8516,.1258,.034,-.0116

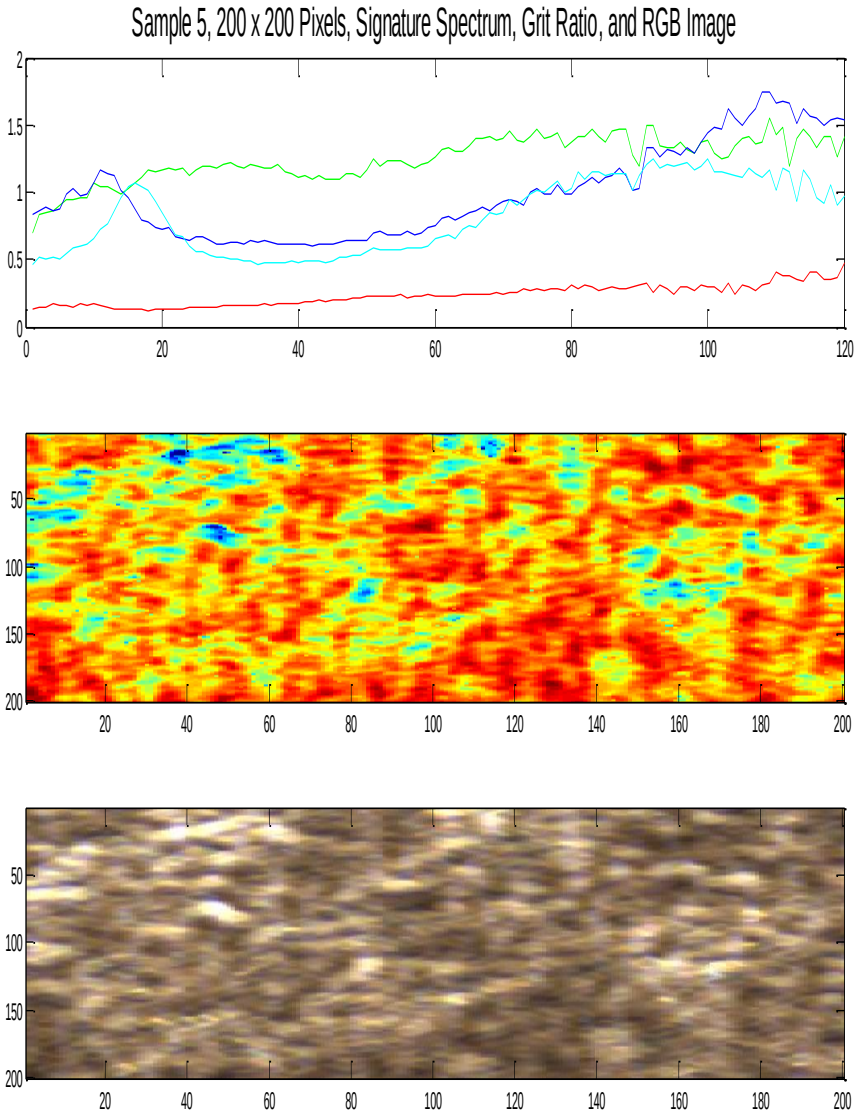

FIGURE 21- SAMPLE 5, 200X200 PIXELS, SIGNATURE SPECTRUM, GRIT RATIO, AND RGB IMAGE

Sample 5							
Location and Size	Grit Ratio	Ratio 2	Ratio 3	Ratio4	Error	Negs	Starting Ratio
(100, 100) – 100x100	.6658	.2795	.0277	.0270	.9971	5526-3318	.6658,.2795,.0277,.027
(100, 200) – 100x100	.5898	.1652	.1489	.0961	.6634	1841-247	.5919,.1676,.1455,.095
(200, 100) – 100x100	.5661	.2086	.1802	.0452	.661	4509-152	.5828,.2662,.163,-.0122
(200, 200) – 100x100	.582	.2187	.1814	.018	.7465	5445-226	.585,.2664,.1978,-.049
(100, 100) – 200x200	.7054	.2256	.0175	.0515	.9051	18189-10626	.7073,.2313,.009,.0524

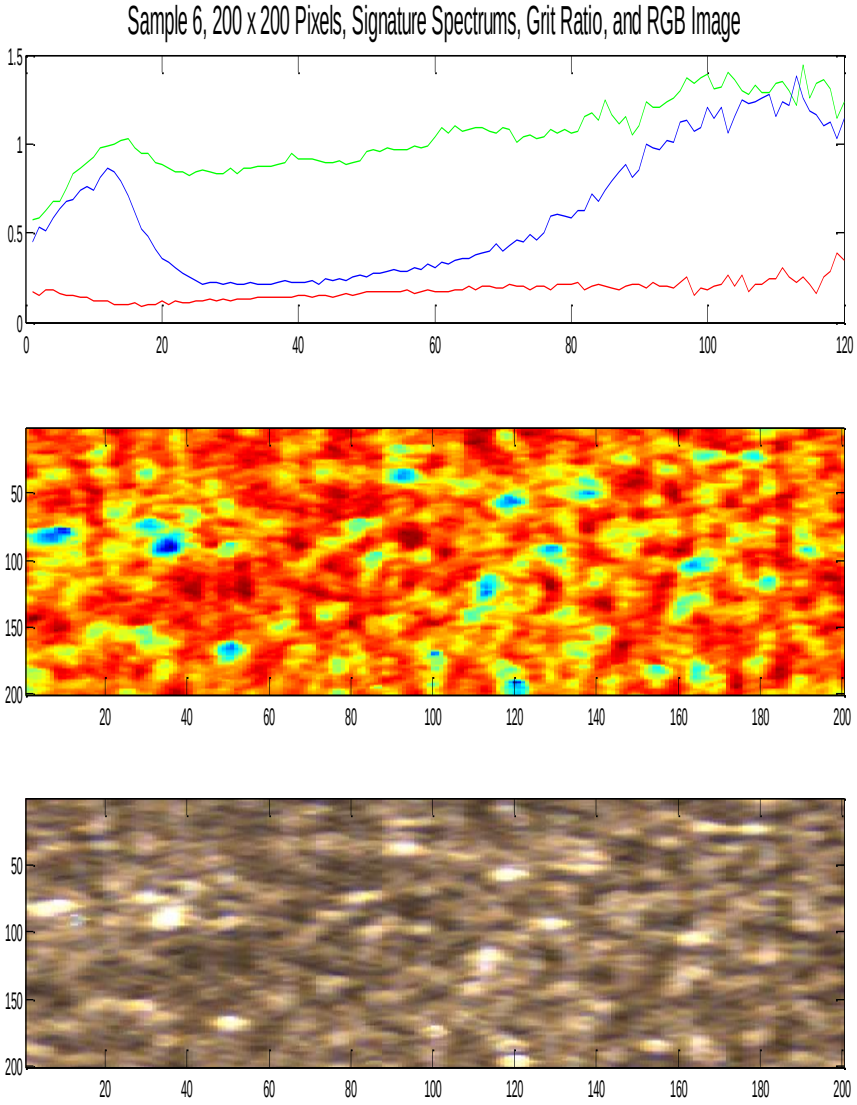

FIGURE 22- SAMPLE 6, 200X200 PIXELS, SIGNATURE SPECTRUMS, GRIT RATIO, AND RGB IMAGE

Sample 6						
Location and Size	Grit Ratio	Ratio 2	Ratio 3	Error	Negs	Starting Ratio
(100, 100) – 100x100	.7151	.1794	.1055	.8619	1625-0	.7232,.1924,.0844
(100, 200) – 100x100	.6235	.1735	.2031	.6886	458-0	.6233,.1714,.2052
(200, 100) – 100x100	.6558	.2235	.1207	.6741	829-0	.6590,.2287,.1123
(200, 200) – 100x100	.6391	.2631	.0978	.5983	328 - 0	.6405,.2655,.0940
(100, 100) – 200x200	.7346	.2357	.0296	1.094	14735 - 0	.7581,.2631,-.0212

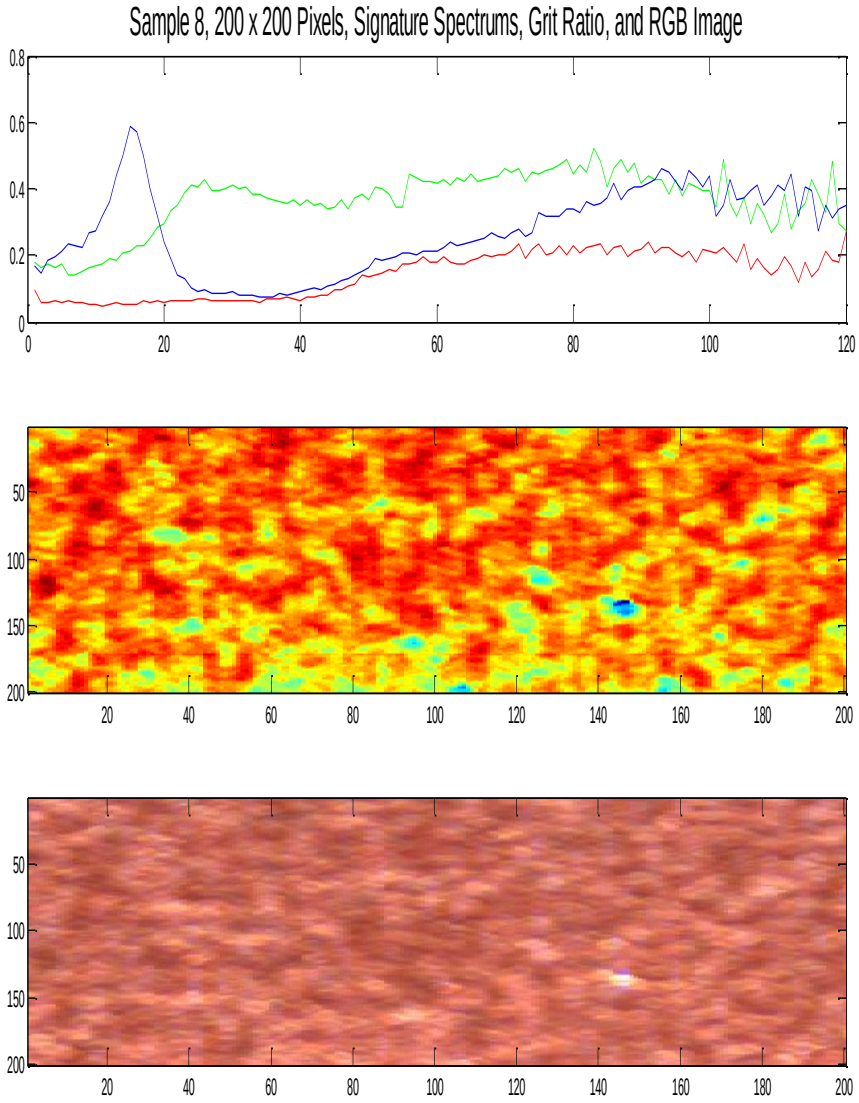

FIGURE 23- SAMPLE 8, 200X200 PIXELS, SIGNATURE SPECTRUMS, GRIT RATIO, AND RGB IMAGE

Sample 8						
Location and Size	Grit Ratio	Ratio 2	Ratio 3	Error	Negs	Starting Ratio
(100, 100) – 100x100	0.6158			.39	0	
(100, 200) – 100x100	0.6728			.38	0	
(200, 100) – 100x100	0.5965			.43	0	
(200, 200) – 100x100	.7359	.132	.1321	.47	2 - 0	.7359,.132,.1321
(100, 100) – 200x200	.7275	.1186	.1539	.487	3 - 0	.7275,.1185,.1540

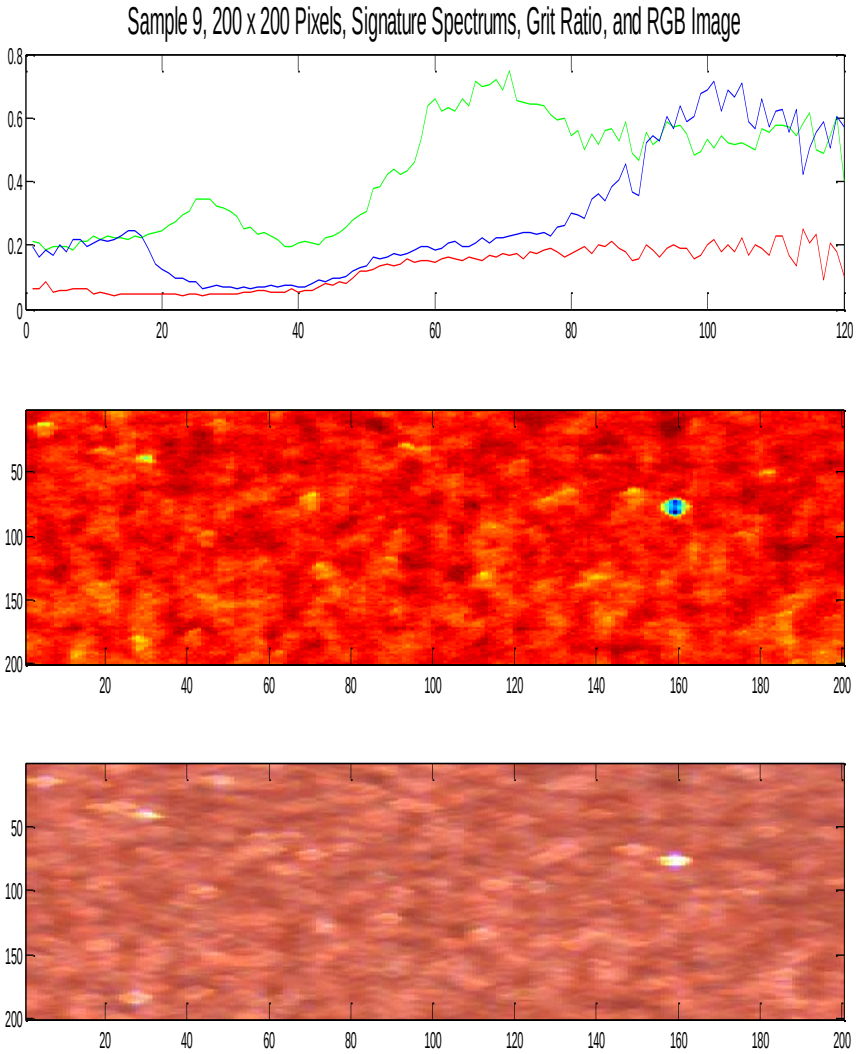

FIGURE 24- SAMPLE 9, 200 X 200 PIXELS, SIGNATURE PIXELS, GRIT RATIO, AND RGB IMAGE

Sample 9						
Location and Size	Grit Ratio	Ratio 2	Ratio 3	Error	Negs	Starting Ratio
(100, 100) – 100x100	.7668			.4146	0	
(100, 200) – 100x100	.8565	.0882	.0553	.3797	21-0	.8567,.0884,.055
(200, 100) – 100x100	.6988			.3775	0	
(200, 200) – 100x100	.6285			.3881		
(100, 100) – 200x200	.8469	.0926	.0605	.3795	59-0	.8471,.0927,.0602

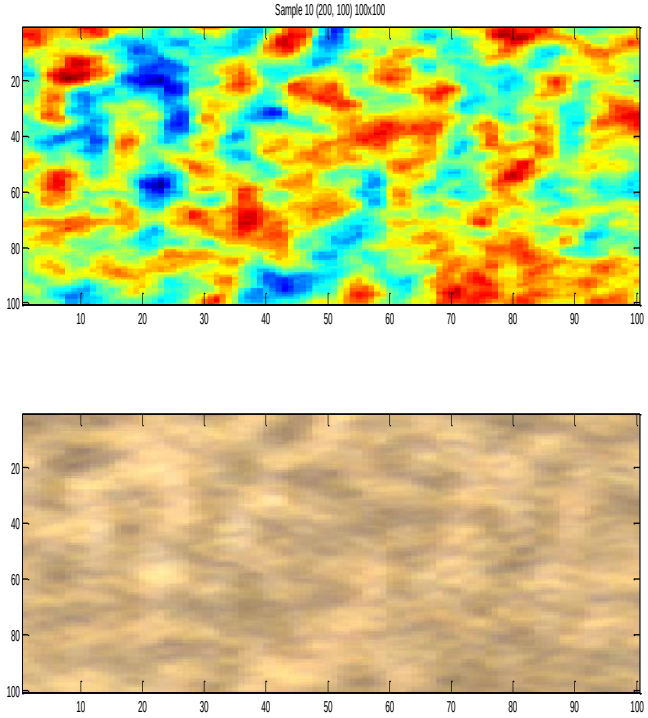

FIGURE 25- SAMPLE 10 GRIT RATIO AND RGB IMAGE

FIGURE 26 – SAMPLE 10 (200,100) 100X100 GRIT RATIO AND RGB IMAGE

Sample 10		
Location – Size	Grit Ratio	Maximum Error of Description
(100, 100) – 100x100	.5544	.4227
(100, 200) – 100x100	.5209	.4556
(200, 100) – 100x100	.5606	.4343
(200, 200) – 100x100	.5066	.4104
(100, 100) – 200x200	.5137	.3928

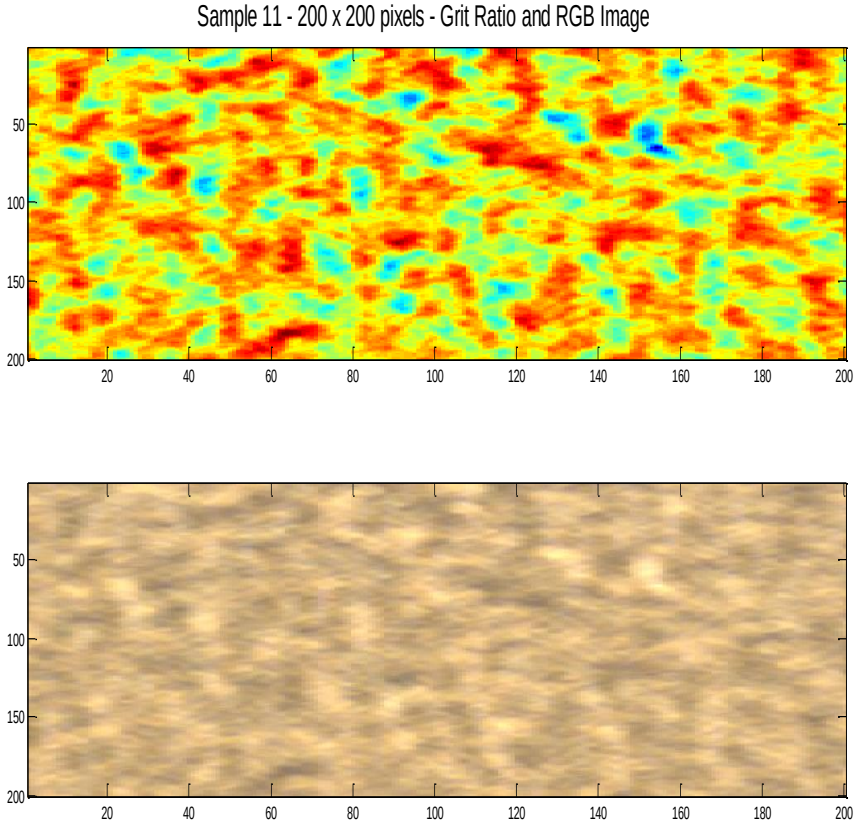

FIGURE 27 – SAMPLE 11, 200X 200 PIXEL REGION, GRIT RATIO AND RGB IMAGE

Sample 11		
Location – Size	Grit Ratio	Maximum Error of Description
(100, 100) – 100x100	0.5778	0.3924
(100, 200) – 100x100	0.6612	0.3934
(200, 100) – 100x100	0.5240	0.3735
(200, 200) – 100x100	0.5584	0.4095
(100, 100) – 200x200	0.6433	0.3906

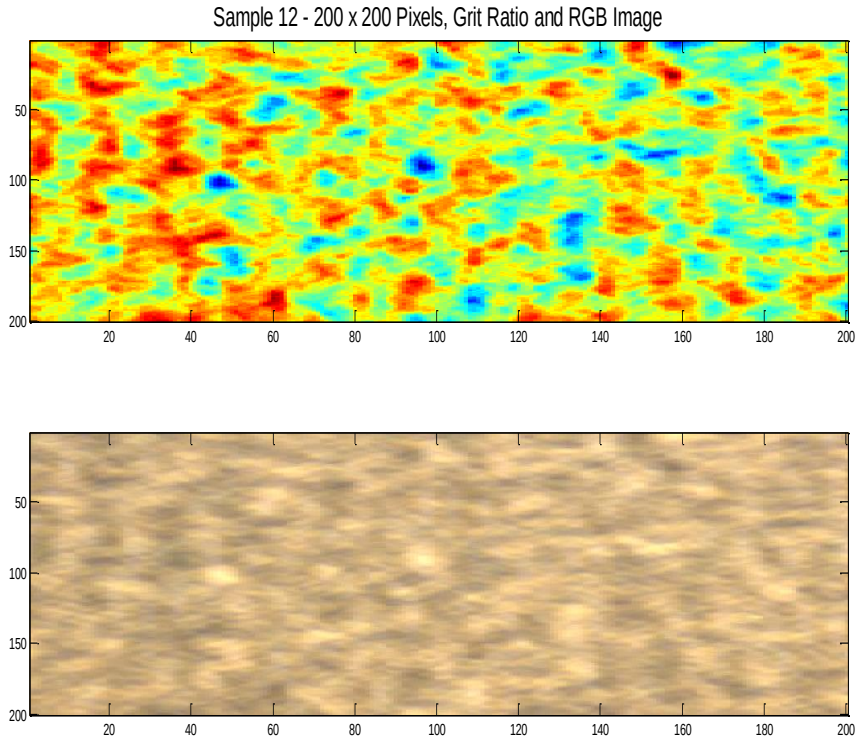

FIGURE 28- SAMPLE 12, 200 X 200 PIXELS, GRIT RATIO AND RGB IMAGE

Sample 12		
Location – Size	Grit Ratio	Maximum Error of Description
(100, 100) – 100x100	0.6178	0.3768
(100, 200) – 100x100	0.5239	0.4119
(200, 100) – 100x100	0.6222	0.3724
(200, 200) – 100x100	0.5754	0.41
(100, 100) – 200x200	.5874	.3828

CONCLUSIONS FROM LINEAR UNMIXING RESULTS

The Modified Fully Constrained Algorithm derived by Chang consistently found abundance fractions that satisfied the sum to one and non-negative constraints when fewer than four abundance fractions were required to accurately describe the pixel vectors in the image. The algorithm was not always capable of satisfying the non-negative constraint when 4 or more target signatures were identified. Sometimes a situation like the one in the following image

would occur where the sum of the absolute values would never equal to 1. Hence, a solution for the Lagrange multipliers could not be found.

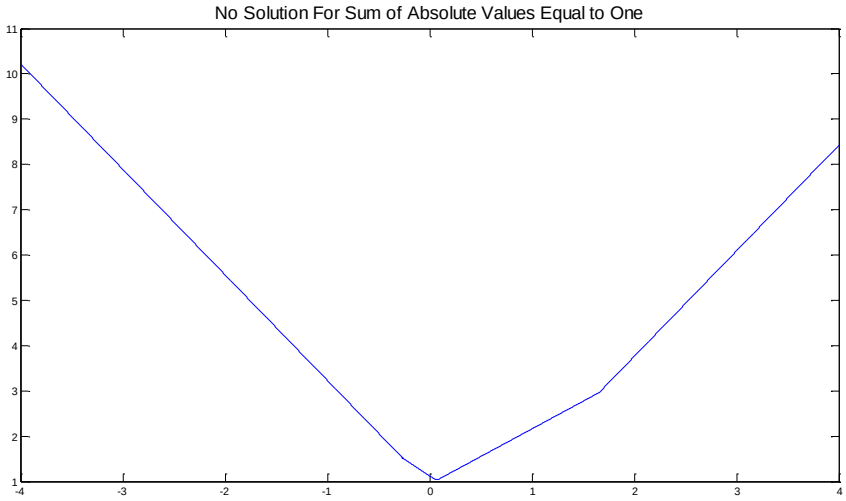

FIGURE 29- NO SOLUTION FOR LAGRANGE MULTIPLIER EXAMPLE

Applying the non-negative constraint did not significantly alter the percentage of grit calculated by the sum to one constrained solution. The Lagrange multiplier algorithm typically adjusted the contribution of the higher reflectance pixel vectors. The proportion of negative abundance fractions was strongly influenced by the presence of abnormally high reflectance pixel vectors in the image.

The linear unmixing results were heavily influenced by anomalous pixel vectors in the image. Some of the images contained pixel vectors that were much higher in reflectance than the other pixel vectors in the image. These pixel vectors were typically created due to the sun's glare reflected by some of the glue areas of the sand paper. Due to the fact that the target selector looked for the extreme pixel vectors, the anomalous pixel vectors were selected to represent glue pixels. The anomalous pixel vectors skewed the linear unmixing such that a larger percentage of the grit target pixel vector was required to describe offset the high energy of the anomalous pixel vector. For example in sample 9, the upper right corner of the image contains an extremely high energy pixel vector. The linear unmixing for this region of the sample identified the percentage of grit coverage at 85%. The lower right corner of sample 9 does not contain any anomalous pixels. The linear unmixing results for this region indicate that the grit coverage is 63%.

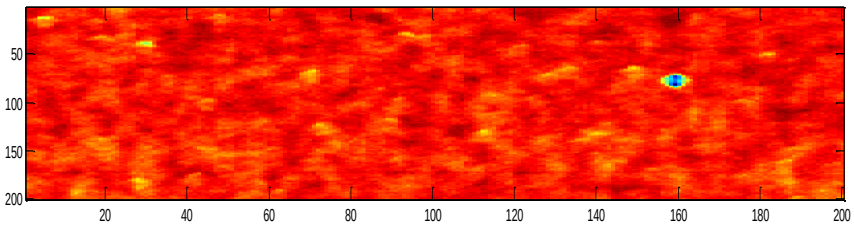

FIGURE 30- SAMPLE 9 GRIT RATIO IMAGE

An attempt to patch the anomalous pixels was made by using the RXD algorithm to identify the pixels that were unusual for the sample. The anomalous pixel vectors were patched with average pixels for the image. The following image shows a patched version of sample 3. The patches are visible in the dark blue areas of the image.

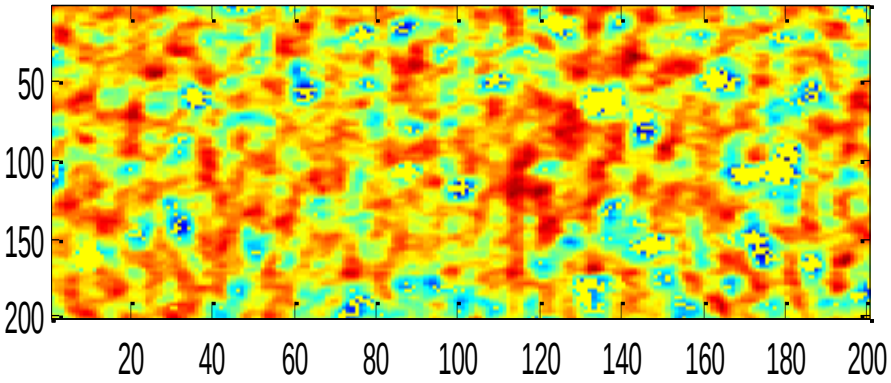

FIGURE 31 – RXD CORRECTED VERSION OF SAMPLE 3

The following chart compares the results of the two equations and two unknowns solution, the MFCL algorithm, and the RXD corrected image with sum to one constrained solution.

Sample Number – Grit Weight	Grit Percentage Two Unknowns	Grit Percentage MFCL Algorithm	Grit Percentage RXD SCL
2 – .105 gms /in^2	66%	73%	70%
3 - .117 gms /in^2	66%	64%	65%
5 – .158 gms /in^2	62%	58%	58%
6 - .215 gms /in^2	63%	64%	63%
8 – .082 gms /in^2	49%	64%	65%
9 - .116 gms /in^2	54%	69%	64%
10 - .036 gms /in^2	46%	.51%	51%

11 - .055 gms /in^2	49%	.55%	58%
12 - .068 gms /in^2	52%	.58%	59%

Samples 10, 11, and 12 are the only group of samples that demonstrated consistent results. These samples are actually the finest grit samples. The highest grit color to the glue color contrast was in samples 5, 6, 10, 11, and 12. These samples also had the most consistent MFCL and RSD SCL results.

CHAPTER 6 - RESEARCH CONCLUSIONS

Three primary methods (DCT Surface Characterization, RXD Variation, and Linear Unmixing) were explored to measure the density of grit application on sandpaper. All three methods were able to provide insight in to the density of grit on the samples.

The DCT and RXD methods demonstrated the potential to determine if a test sample varied significantly from a known good sample.

The linear unmixing algorithms demonstrated the potential to determine the grit density without any prior knowledge of the sample being examined.

The linear unmixing algorithms only produced repeatable results on the 80 grit and 120 grit samples. Linear unmixing for the 40 grit and 50 grit samples did not produce the expected results. Unfortunately, the lower density 40 and 50 grit samples contained significant amounts of glare that may have compromised the results. The linear unmixing results showed that the grit application was not uniform for any of the grit sample types.

For the RXD algorithm approach, the standard deviation of the samples decreased with more grit. The glue areas produced the greatest variation. If the sample was composed of mostly mixed grit and glue pixels, the standard deviation dropped. Attempts to create a tailored covariance matrix for the RXD algorithm did not produce results that converged to a meaningful determination of grit density.

Perhaps the most robust results were accomplished with the Direct Cosine Transform surface frequency characterization algorithm. The algorithm consistently identified a difference in the surface between known good samples and a target sample. The reflectance magnitude variation caused by exposure time may be an issue with this method though.

A hyperspectral camera may be difficult to implement on a high speed web application, but most of the algorithms demonstrated the same level of success with a simulated RGB approach. The following RGB camera system bill of material would provide a strobed high speed camera system that would support further testing of the algorithms identified in this research.

K56-999 - $650- 4000 Strobe Controller
Output for one light head, 1 microsecond minimum pulse

K55-813 - $696 – RGB Ring Light
4 inch working distance, 1.7” coverage,

NT63-856 - $1,195 - EO-3112C Color GigE Camera
½” progressive scan CMOS Micron MT9T001 sensor, 2048 x 1536 pixels.

NT59-233 - $60 – Cat6 Ethernet Cable, 25 ft

NT63-866 – $65 – Intel PRO/100 Video Capture Board

NT58-001 - $250 – Techspec Compact 12 mm Focal Length Lens

NT03-632 - $5.95 – 1 mm Spacer

NT03-631 - $5.95 – ½ mm Spacer

BIBLIOGRAPHY

Gonzalez, Rafael C. and Woods, Richard E. . Digital ImageProcessing. Prentice Hall, 2002.

Chang, Chein-I. Hyperspectral Imaging, Techniques for Spectral Detection and Classification. Kluwer Academic/Plenum Publishers, 2003.

Tao Xin, Fan Wenjie, Xu Xiru. Blind Separation of Component Information from Mixed Pixels in Hyperspectral Imagery. National Natural Science Foundation of China, 2007.

deJong, Steven M. and van der Meer, Freek D., Remote Sensing Image Analysis. Kluwer Academic Publishers, 2004.

Chen, C. H.. Signal and ImageProcessing for Remote Sensing. Taylor and Francis Group, 2007.

Kanellopoulos, I, Wilkinson, G., Moons, T., Vision and Advanced Image Processing in Remote Sensing, 1999.

Borengasser, M., Hungate, W. S.,Watkins, R.. Hyperspectral Remote Sensing, Principles and Applications, 2008